HHS Public Access

Author manuscript

Acta Biomater. Author manuscript; available in PMC 2020 October 01.

Published in final edited form as:

Acta Biomater. 2019 October 01; 97: 513–523. doi:10.1016/j.actbio.2019.07.020.

Mechanics of Pulmonary Airways: Linking Structure to Function Through Constitutive Modeling, Biochemistry, and Histology

Mona Eskandari[a,b,d,e], **Tara M. Nordgren**[c,d], **Grace D. O'Connell**[e,f]

[a]Department of Mechanical Engineering, University of California at Riverside, Riverside CA, 92521

[b]Department of Bioengineering, University of California at Riverside, Riverside CA, 92521

[c]Division of Biomedical Sciences, University of California at Riverside, Riverside CA, 92521

[d]BREATHE Center School of Medicine, University of California at Riverside, Riverside CA, 92521

[e]Department of Mechanical Engineering, University of California at Berkeley, Berkeley CA, 94720

[f]Department of Orthopaedic Surgery, University of California at San Francisco, San Francisco CA, 94143

Abstract

Breathing involves fluid-solid interactions in the lung; however, the lack of experimental data inhibits combining the mechanics of air flow to airway deformation, making it difficult to understand how biomaterial constituents contribute to tissue response. As such, lung mechanics research is increasingly focused on exploring the relationship between structure and function. To address these needs, we characterize mechanical properties of porcine airways using uniaxial tensile experiments, accounting for bronchial orientation- and location dependency. Structurally-reinforced constitutive models are developed to incorporate the role of collagen and elastin fibers imbedded within the extrafibrillar matrix. The strain-energy function combines a matrix description (evaluating six models: compressible NeoHookean, unconstrained Ogden, uncoupled Mooney-Rivlin, incompressible Ogden, incompressible Demiray and incompressible NeoHookean), superimposed with non-linear fibers (evaluating two models: exponential and polynomial). The best constitutive formulation representative of all bronchial regions is determined based on curve-fit results to experimental data, accounting for uniqueness and sensitivity. Glycosaminoglycan and collagen composition, alongside tissue architecture, indicate fiber form to be primarily responsible for observed airway anisotropy and heterogeneous mechanical behavior. To the authors' best knowledge, this study is the first to formulate a structurally-motivated constitutive model, augmented with biochemical analysis and microstructural observations, to investigate the mechanical function of proximal and distal bronchi. Our systematic pulmonary tissue characterization provides a necessary foundation for understanding pulmonary mechanics; furthermore, these results enable clinical translation through

eskandar@ucr.edu.

simulations of airway obstruction in disease, fluid-structure interaction insights during breathing, and potentially, predictive capabilities for medical interventions.

Keywords

Lung Mechanics; Biochemistry; Histology; Material Behavior; Constitutive Modeling; Tissue Characterization

1. Introduction

Billions of dollars are spent annually treating lung disease, which is the leading cause of death worldwide (6; 70; 89). Chronic obstructive pulmonary disease alone claims three million lives each year (24). The lung is a fluid-structure system, but current lung biome chanics research consists predominantly of single-mechanism approaches, where the fluid mechanics community explores fluid flow, particle deposition, and branching algorithms (25; 46; 49; 52; 62; 88; 93; 90), and the solid mechanics community investigates trachea, alveolar, and parenchymal tissue response (39; 58; 59; 67; 83). The lack of experimental data on lung tissue mechanics limits research efforts in modeling airway obstruction behavior due to inflammation or constriction, or tissue remodeling in chronic lung diseases (e.g., asthma or bronchitis). Existing computational studies have been constrained to oversimplification of tissue material properties (19; 20; 42; 45; 55; 87), or restricted to the trachea due to the challenge of acquiring intra-parenchymal bronchi material properties (14; 74; 81; 82). Analogously, unknown pulmonary mechanics cause majority of fluids research to simulate flow through rigid airways (62; 69; 88), despite knowing that accounting for tissue deformations will significantly change airflow patterns, which is even more pronounced in diseased states (53; 85; 94). Experimentally informed mathematical models representative of airway behavior are capable of integrating pulmonary fluid and structure systems to investigate healthy and diseased lung function.

Our recent work experimentally measured uniaxial tensile mechanics of porcine bronchi, demonstrating material region-dependency from proximal to distal airways (23). Circumferentially oriented specimens were nearly twice as stiff in distal airways than proximal airways. Furthermore, stiffness of axially oriented specimens were almost double that of circumferentially oriented specimens; Anisotropy agreed well with fiber orientation, which was primarily aligned in the axial direction. These experimental observations are critical to developing constitutive models of bronchial mechanics.

Research on other fiber-reinforced biological structures, such as cardiovascular tissue or annulus fibrosus of the intervertebral discs, have successfully described bulk tissue mechanics through structural constitutive laws (3; 63; 73; 84; 86). These models have been able to describe the relative stress contribution of each tissue subcomponent, including fibers, extrafibrillar matrix, and their interactions. Moreover, these models have been used to accurately describe the material response under other loading modalities, such as simple shear, which is difficult to measure experimentally due to the lack of fiber engagement (10; 40; 65). However, identifying appropriate constitutive laws without over-constraining or over-parameterizing the model has not been trivial.

The progression of lung research relies on establishing and accurately representing bronchial tissue biomechanical properties (45; 78). Thus, the aim of this study is to develop a structure-based constitutive model describing uniaxial mechanical behavior of proximal and distal airways. Additionally, the biochemical composition for each tissue region is assessed to investigate how individual mechanical constituents impact bulk tissue behavior. Lastly, histology is performed on the trachea, large bronchi, and small bronchi to determine the influence of fiber architecture on mechanical function.

Robust computational models are valuable for understanding three-dimensional deformations in healthy and diseased lungs, and eliciting similarities between porcine and human tissues can facilitate such insights (41; 61; 57). Results from this study provide important information for constructing physiologically relevant models that represent native tissue anisotropy and heterogeneity. Most importantly, the formulated constitutive model in this study enables the connection of air flow forces to deformations, advancing comprehensive fluid-structure analyses, which impeded pulmonary biomechanics research to date.

2. Materials and Methods

2.1. Lung Specimens

Specimen preparation is briefly described here as experimental characterization was the focus of previous work and is used to inform the constitutive model described here. For more details on tissue preparation, protocol development, and mechanical testing, the reader is directed to Eskandari et al. 2018 (23).

Uniaxial tensile tests were performed on specimens from the trachea, large bronchi, and small bronchi of porcine lungs (n = 27–30 per lung, Figure 1A). Animals were obtained from an abattoir and did not require IACUC approval (n = 5 animal lungs). Bronchi have a cartilaginous layer wrapped around soft tissue, which forms the innermost layers (mucosa and submucosa) (5; 19). Cartilage morphology evolves from a C-ring in the trachea to individual scales distally; samples were consistently collected from proximal and distal regions with disconnected cartilage sections and freely deforming soft tissue to isolate and examine the mucosa and submucosa layers only (18). The specimens were oriented along the airway's circumferential or axial direction (Figure 1B) (14; 60). Experimental protocol development and consistent tissue handling technique is critical to proper material measurement (23). The biomechanics literature lacks a universal gripping technique or soft tissue tare load (pre-load) procedure to replicate *in vivo* physiological forces, despite the known impact on measured stress-strain behavior. As a common tare load was inappropriate for samples of varying location and orientation, the unloaded reference state was defined after data collection to consistently locate the initial state on the classical J-shaped curve (using mathematical analysis of curve concavity (23)). Rectangular test specimens (dimensions: 4.4±1.0 mm wide, 6.4±1.9 mm long, and 2.0±0.6 mm thick) were strained to 35% at a rate of 1%/sec for six cycles and the loading stress-strain response from the last cycle was analyzed (Figure 1C) (23; 81).

2.2. Continuum Mechanics

Non-linear constitutive equations were used to mathematically describe tissue deformations based on experimental results. The deformation map $\phi(X)$ related the undeformed state to the deformed state, and the deformation gradient, $F(X)=\nabla\phi(X)$, was defined as a diagonal matrix for uniaxial tensile testing (33; 74):

$$F = \begin{bmatrix} \lambda_1 & 0 & 0 \\ 0 & \lambda_2 & 0 \\ 0 & 0 & \lambda_3 \end{bmatrix} \quad (1)$$

λ_1, λ_2 and λ_3 were principle stretches and λ_3 was aligned with the elongation direction of the tissue (Instron 5848 Microtester). λ_3 was described as $\lambda_3 = 1 + d/L$, where d was the displacement normalized by the initial length L. λ_1 and λ_2 were assumed to contract equally, according to the Poisson's ratio ν, which was a free parameter for compressible strain-energy models. The deformation gradient for large deformations was generalized by using Poisson's ratio to account for transverse direction contractions (Equation 2). F was further reduced to $F = diag\left(\sqrt{\lambda_3}; \sqrt{\lambda_3}; \lambda_3\right)$ for incompressible models (i.e., $\nu = 0.5$) (34).

$$F = \begin{bmatrix} \lambda_3^{-\nu} & 0 & 0 \\ 0 & \lambda_3^{-\nu} & 0 \\ 0 & 0 & \lambda_3 \end{bmatrix} \quad (2)$$

2.3. Constitutive Models

Observations of anisotropic microstructure and inspection of tissue morphology informed fiber orientation and motivated our use of a structurally defined strain-energy density function (SED) (9; 32; 44). SED functions commonly found in the literature, expressed in terms of material parameters and invariants of the deformation tensor, are listed in Table 1. Six phenomenological hyperelastic constitutive models were assessed as a potential description for the extrafibrillar matrix (11; 13; 71). They differ in representing both compressible and incompressible behaviors, the degree of non-linearity representation (i.e. stretch raised to a power, acting within an exponential, or as an inverse), and number of fitted parameters. Some expressions were originally formulated for rubber-like materials and others for soft biological tissues, and all have precedent for use in formulating new constitutive relationships (10; 29; 51).

Once a constitutive relationship was defined for the matrix, it was augmented with a non-linear stress-stretch description for the fibers, as axial tissues displayed greater strain-stiffening well represented by exponential or polynomial expressions (Figure 2) (29; 79). It was assumed that only the extrafibrillar matrix was engaged for specimens tested along the circumferential direction, and testing along the axial direction engaged fibers embedded within the matrix (Figure 1D, Equations 3–4) (34; 35; 38; 73).

$$\psi_{\text{circumferential}} = \psi_{\text{matrix}} \tag{3}$$

$$\psi_{\text{axial}} = \psi_{\text{matrix}} + \psi_{\text{fiber}} \tag{4}$$

For clarity, only the derivation of the first Piola-Kirchhoff stress, P, for the compressible Neo-Hookean strain-energy is described here (Equations 5–6); the same procedure was followed for all constitutive relationships (21). Briefly, P was found by deriving the strain-energy function with respect to F using chain and product rules. Experimental P, P^{exp}, was directly measured from uniaxial tensile tests (54), where $P^{\text{exp}} = f_z/(WT)$; f_z was the force measured by the load cell, W represents tissue width, and T represents tissue thickness. J is defined the determinant of F (36).

$$\psi(I_1(\lambda_3), J(\lambda_3)) = \frac{1}{2}\mu[I_1 - 3] + \frac{\lambda}{2}\ln(J)^2 - \mu\ln(J) \tag{5}$$

$$P = \frac{\delta\psi_{\text{C-NH}}}{\delta F} = \frac{\delta\psi_{\text{C-NH}}}{\delta I_1}\frac{\delta I_1}{\delta\lambda_3}\frac{\lambda_3}{\delta F} + \frac{\delta\psi_{\text{C-NH}}}{\delta J}\frac{\delta J}{\delta\lambda_3}\frac{\lambda_3}{\delta F} \tag{6}$$

Partial derivatives terms were (79):

$$\frac{\delta\psi_{\text{C-NH}}}{\delta I_1} = \frac{\mu}{2};$$
$$\frac{\delta I_1}{\delta\lambda_3} = -4\nu\lambda_3^{(-2\nu-1)} + 2\lambda_3;$$
$$\frac{\delta\psi C - NH}{\delta J} = \frac{\mu}{J} + \frac{\lambda}{J}ln(J);$$
$$\frac{\delta J}{\delta\lambda_3} = (1-2\nu)\lambda_3^{-2\nu};$$
$$\text{and } \frac{\lambda_3}{\delta F} = 1.$$

Viscous and porous effects were ignored; however, unlike biological studies where compressibility was commonly assumed *a priori*, here compressibility was an output of the curve-fitting process (51; 54). Preliminary digital image correlation results substantiated the assumption of homogenous uniaxial tissue deformation (23).

2.4. Material Model Calibration

MATLAB's non-linear least squares algorithm, *lsqnonlin*, was used to minimize the difference between model generated P and P^{exp}. Experimental data was interpolated into 1001 equally spaced points to avoid curve-fit biasing. Upper and lower bounds were set to $\pm\infty$ for all parameters, except ν, which was constrained between 0 and 0.5, and c_2 in the uncoupled Mooney-Rivlin model, which was negative for concavity (33). Each parameter's initial guess was randomized, varied two orders of magnitude, and subject to multiple runs to check for uniqueness in the resulting model parameters.

A Bland Altman analysis was used to provide a measure of agreement between model and experimental data. The coefficient of determination provided goodness of fit and was defined as $R^2 = 1 - S^{\text{residual}}/S^{\text{total}}$, where $S^{\text{residual}} = \Sigma_i^{1001}\left(P_i^{\exp} - P_i\right)^2$, and S^{total} with $P_{\text{mean}} = \Sigma_i^{1001}\left(P_i^{\exp} - P_{\text{mean}}\right)^2$, as the mean of observed data (10). The best-fit model was defined as the one with the smallest mean for residual error $\Sigma_i^{1001}\left(P_i^{\exp} - P_i\right)$ in conjunction with an R^2 value closest to 1.0. The adjusted R^2 was also considered to account for comparing models with differing number of parameters, but the difference observed was negligible (R^2 differed by 10^{-5}).

Once matrix parameters were determined (Equation 3), the stress-stretch data for axial specimens were curve-fit to the matrix and fiber description (Equation 4). Results from circumferential direction specimens were used to determine the upper and lower bound for the matrix parameter curve-fit in the axial direction (bounds = average ± 1 standard deviation; Figure 1D). Thus, the best-fit structurally-reinforced constitutive model representative of all three regions (trachea, large bronchi, and small bronchi) was determined. Matrix and fiber stress contribution was calculated by dividing the stress for each subcomponent by the total stress across the strain range for axial tissues (31).

2.5. Sensitivity Analysis

A sensitivity analysis was conducted to inform how deviations in constitutive model parameter calibrations influenced the stress-stretch response (31; 64). For circumferentially oriented samples fit to the incompressible Demiray model, one parameter, either μ or β, was fixed at the average value, while the other parameter was varied between average ±1 standard deviation. Similarly, for axial samples augmented with an exponential fiber function, μ, β, k_1 or k_2 were varied between average ±1 standard deviation, while the other three parameters were held at their average value.

2.6. Biochemistry

A single porcine lung was used to quantify biochemical composition for the trachea, large bronchi, and small bronchi. A 4 mm diameter biopsy punch was used to prepare three specimens at each location. A scalpel was used to separate the cartilage layer from soft tissue. Samples were weighed to acquire wet weights and then dried overnight in a lyophilizer to measure dry weights before digesting the tissue in 1 mL of 0.5 mg/mL proteinase K (56°C).

Water content was calculated as the difference between wet and dry weights normalized by the wet weight. DNA content was determined using the PicoGreen Kit (Invitrogen). Glycosaminoglycan (GAG) content was determined using 1,9-dimethylmethylene blue (DMMB). A 100μl aliquot of the digested sample was prepared for the hydroxyproline assay through acid hydrolysis (12 M HCl). The ratio of hydroxyproline to collagen was assumed to be 10.0.GAG and collagen contents were normalized by wet weight, dry weight, and DNA content (8).

2.7. Histology

A representative specimen from the trachea, large bronchi, and small bronchi region was prepared for histological staining. Specimens were cut from the airway using a scalpel, fixed in 4% formaldehyde solution (66), and sent to Gladstone Institutes Histology and Light Microscopy Core (University of California, San Francisco) for processing, sectioning, and staining. Dehydrated samples were embedded in paraffin wax blocks and two serial 10 μm thick slices were collected onto glass slides. Sections were axially prepared, as samples displayed axially aligned collagen and elastic fibers (undiscerned between types of collagen or elastic, elaunin, and oxytalan fibers (9)). Samples were stained with Masson's Trichrome to visualize the tissue architecture (9; 72), where red stained elastin and blue stained collagen (16). Slides were imaged with a digital camera (AmScope FMA037, Irvine CA) attached to an upright microscope (Olympus CKX31).

2.8. Statistics and Correlations

MATLAB was used to identify statistical outliers, which were defined as values exceeding 150% of the interquartile range (Statistics Toolbox, Mathworks Inc.). All values were subject to a Box-Cox transformation to account for non-normal distribution, followed by a one-way analysis of variance (ANOVA) and Bonferroni post-hoc analysis. Spearman's correlation (ρ) was performed to find potential interparameter dependencies, and dependencies between model parameters and experimentally measured mechanical properties (23). Thresholds for strong, moderate, and weak correlations were defined as $\rho \geq 0.7$, $0.7 > \rho > 0.5$, and $\rho \leq 0.5$, respectively (15). Significance was set at $p < 0.05$ for all analyses. Bulk tissue stiffness modulus, E, was defined as the slope of stress-strain curve in the toe-region (23), which was found to be significantly correlated to constitutive parameters, and thus, subjected to further relational analyses (31; 64).

3. Results

3.1. Constitutive Model Performance

Specimens tested along the axial direction displayed consistently greater stresses for given strain range than specimens tested along the circumferential direction (Figure 2). Axial-direction stiffness did not depend on spatial location, but the stiffness of circumferential specimens from the small bronchi was greater than the trachea ($p < 0.01$ and large bronchi ($p < 0.05$) (23).

Five of the six matrix models had R^2 values greater than 0.95. The incompressible Neo-Hookean model did not describe experimental data well ($R^2 = 0.82$, Table 1; Figure 3B-C), as it was incapable of capturing the non-linear stress-stretch response with a single parameter. Uniqueness evaluations found compressible models were generally over-parameterized, resulting in non-unique curve-fits. Thus, the incompressible Demiray model was determined to be the best matrix model with the highest R^2 value, minimum residual error ($R^2 = 0.997$, residual=−0.041 MPa), and to be unique, followed by the incompressible Ogden model (Table 2.6, green highlighted models).

After the matrix model was selected, stress-stretch data from axially oriented samples were fit to a 2-term exponential or polynomial strain-energy function to describe fiber mechanics. Residual error was lower and R^2 values were greater for the exponential description (R^2 = 0.991, residual=−0.175 MPa; Table 2.6). Therefore, the combined strain-energy function was an incompressible Demiray matrix description with an exponential expression for the fibers, resulting in four model parameters: μ and β for the matrix parameters, and k_1, and k_2 for the fibers (Figure 4), similar to the two-term exponential form introduced by Humphrey and Yin (38).

3.2. Region-Dependent Mechanical Behavior

Matrix parameters were informed by experimental data from both circumferential and axial direction specimens, which led to observed differences in the magnitude of these parameters. However, similar trends were expected and seen with respect to region, where μ was greatest for the small bronchi and β was greatest for the large bronchi ($p<0.01$). k_1 and k_2 decreased from the trachea to the small bronchi ($p<0.01$; Figure 4).

The matrix contribution to uniaxial loading was significantly lower in the trachea and large bronchi (29±19% and 32±16%, respectively) than the small bronchi (50±28%; $p<0.002$). Stress contribution in the trachea and large bronchi was mostly carried by the fibers (71±19% and (68±16%), while fiber and matrix contribution was nearly equal in the small bronchi (Figure 5).

3.3. Correlations to Material Properties

Table 3 reports inter-relationships between model parameters, and correlations between model parameters and measured bulk tissue modulus (E). At the initiation of tissue deformation λ_3=1, μ physically represents the matrix stiffness and k_1 represents the fiber stiffness; β and k_2 define material non-linearity. The only inter-parameter correlation found was between β and k_2 and was very weak (ρ = −0.25, p=0.02); thus, inter-parameter relationships were not further analyzed. In the circumferential direction, E was strongly correlated to μ (ρ>0.9, p=0; Figure 6), with a weak, but significant, correlation to β (ρ=0.26, p=0.02). In the axial direction, there was a weak correlation between E and μ (ρ=0.43, p=0), and a strong correlation between E and k_1 (ρ=0.79, p=0; Figure 6). The slope of $E-\mu$ response was observed to be nearly half that of the $E-k_1$ trend.

3.4. Sensitivity Analysis

Sensitivity analysis explored how model performance was impacted by variations in determined model parameters (Figure 7). Greater sensitivity was defined as a wider deviation in stress response for a given stretch. Generally more variation from the average response was seen with increased stretch. Stress-stretch behavior for the small bronchi was most sensitive to μ and β. Stress-stretch results for the trachea and large bronchi were more sensitive to fiber parameters k_1 and k_2, than matrix parameters. With respect to regional variations, the small bronchi was almost equally sensitive to matrix and fiber parameters, relating to the equal contribution observed in the overall stress response (Figure 5). k_1 and μ resulted in the most sensitivity for axial and circumferential specimens, respectively.

3.5. Tissue Composition and Microstructure

Regional variations in GAG and DNA content normalized by dry weights were observed, where the GAG content in the trachea (0.3± 0.5%) was significantly lower than large; (2±0.1%, p=0.001) and small bronchi (2 ± 0.04%, p<0.001;.Figure 8). There were no significant differences in overall collagen content with respect to airway region (p≥0.07, trachea: 14 ±2%; large bronchi: 10±3%; and small bronchi: 17 ± 2%). However, Masson's Trichrome staining suggests regional differences between fiber architecture (collagen and elastin; Figure 9). Within the mucosa layer (5), fibers displayed notable crimping for trachea regions and were more taut distally (i.e., small bronchi).

4. Discussion

In this study, we have established the first experimentally informed constitutive model for extra- and intra-parenchymal airways. The structure-based model represents bulk tissue anisotropy by describing non-linear fibers imbedded in the extrafibrillar matrix. Notable bronchial heterogeneity observed in experimental data manifests in the constitutive model as varying parameter values. Good agreement with experimental data and strong correlations between bulk tissue modulus and model parameters for matrix and fiber stiffness demonstrates accurate representation via a non-interacting fiber-matrix description (Figure 6) (31; 65). Describing bronchial tissue as incompressible is also found to be adequate (Table 2.6) (11; 54).

Differences between trachea and small bronchi mechanics are significant across all constitutive model parameter fits (Figure 4). In contrast to experimental observations where significant regional dependency was seen only in circumferential samples, our constitutive model highlights axial tissue heterogeneity. Fiber parameters k_1 and k_2 decreased distally unlike matrix parameters μ and β, which displayed heterogeneity but not unidirectional trends (Figure 4).

Individually calibrated parameters do not directly manifest in bulk tissue response but match the overall stress contribution trends from proximal to distal regions (Figure 5): highest matrix stiffness, as seen in the small bronchi, corresponds with greatest matrix stress contribution; similarly, high fiber stiffness translates to greater fiber stress contribution in the trachea and large bronchi. The increasing role of the matrix contribution distally is important in diseased states, as previous studies have shown the matrix to be responsible for triggering tissue remodeling (17; 30). Our model could be used to study remodeled states through altered matrix and fiber stiffness.

In selecting an appropriate combination of SED functions to describe airway mechanics, sensitivity and uniqueness were evaluated to ensure that the selected model was not over-parameterized or over-sensitive to one particular parameter. Deviation in model fit to experimental data indicates some model parameters to be more sensitive than others (Figure 7). Greater sensitivity corresponds to decreased model fidelity, with more sensitive parameters causing more variability in predicted tissue behavior. Regional sensitivity appears to trend with stress contribution: matrix stress-strain response is increasingly more sensitive to matrix parameters distally (in both axial and circumferential samples), which

also corresponds to the tissue region with greatest matrix contribution. Greater sensitivity to fiber parameters is similarly observed in axial trachea and large bronchi specimens, corresponding to regions with greatest fiber contribution.

The datasets for matrix modulus (μ) and fiber modulus (k_1) were from circumferential and axial samples respectively, and their direct positive relationship to E is expected from model construction; however, the differing degree of μ and k_1 correlation with E suggests changes in the matrix modulus less drastically impacts the overall bronchial stiffness, whereas slight changes in fiber modulus would more greatly influence tissue behavior. This indicates that while initial isotropic models helped understand airway obstruction (20; 22; 56; 87), the role of fibers is critical and must be considered in bronchial mechanics.

The association between tissue composition and mechanics is considered. GAGs are coupled to viscoelasticity, resist elongation, and display a stepwise concentration increase from the trachea to the small bronchi (Figure 8) (30). μ is the greatest in the small bronchi but does not continuously increase distally as GAG does. The higher concentration of GAG in small bronchi may resist loading deformations more, resulting in greater stress range and increased matrix contribution distally. Moreover, GAG correlates to energy dissipation: a previous study showed GAG degradation caused increased energy dissipation (1); therefore, one could postulate the increased presence of GAG translates to greater energy efficiency for smaller airways. Our upcoming viscoelastic models better explain the observed heterogeneous stress relaxation (23) and explore the energy efficiency of bronchi.

Contrary to GAG content, collagen is homogenous throughout the airway, unlike fiber parameters k_1 and k_2, which decreased from the trachea to small bronchi (Figure 4 and 8). This difference may be due to limits of measuring hydroxyproline, a molecule that is part of fibrous components that may not directly contribute to tensile mechanics (e.g., elastin or minor collagens) (7). Nonetheless, taken together, these findings provide preliminary support for linking quantitative measures of tissue composition with model parameters, which will be important for understanding tissue remodeling with age and disease (68). Future work will need to assess specific proteins to inform the relationship of fibrous composition to mechanical properties, and how that may evolve in disease.

Collagen and elastin fibers are the major force-bearing pulmonary components (27): collagen fibers are inextensible, stretching 2%, while elastin fibers can stretch 140% (77). The intimate association of these fibers and arrangement throughout the lungs dictates expansion (2). However, the inconclusive correlation of homogenous collagen content to heterogenous constitutive material properties suggests tissue composition alone may not be primarily responsible for mechanical function.

Investigating regional tissue microstructure through histology yields qualitative insights of bronchial fiber evolution, which is unestablished to date (Figure 9) (44). Fibers appear uniformly axially aligned, with dispersion unlikely to influence mechanical function, in contrast to arterial tissue (29; 35). Collagen and elastin fibers evolve from crimped to taut. Curling is more prominent in the trachea and large bronchi, whereas small bronchi fibers have limited curvature. The heterogenous fiber architecture is morphological and is not

attributed to *ex vivo* experimental effects because residual stresses are not observed in pig bronchi (57; 80).

The curve and weave of fibers are key to elastic properties, enabling tissue stretch despite the relative inextensibility of collagen fibers (28; 92). Folded collagen in proximal airways initially undergo straightening and are more compliant when elongated, enabling expansive range of stretch toleration with reduced stress range. Straightened fibers in distal small bronchi reach non-physiological strains sooner, translating to heightened relative levels of stress (Figure 7) (23). The heterogeneity of model parameters and histology confirm conjectures surrounding raised stresses caused by lung inhomogeneity (30), and should be considered in circumstances such as artificial ventilation, where overextension has been identified to induce inflammatory response and trigger remodeling (43).

Collagen-elastin fiber form in differentiating bronchial regions also relates to disease etiology. It is well recognized that environmental exposures such as cigarette smoke, mineral dust exposures, and lung infections alter the extracellular matrix composition and contribute to resulting disease (37; 75; 77). Mechanisms include tissue degradation, superfluous matrix deposition during repair, and immune response activation that leads to further tissue damage. Remodeling of tissue caused by disease has been considered to reorient collagen (91) and degenerate elastin (4; 22; 26; 42; 55). Analogous to computational fluid dynamics models which have already made progress in predicting restricted flow in diseased airways (47), it is prudent to characterize the changing form and architecture of the extracellular matrix throughout the lung in order to better understand how pathologies impacts normative and pathological lung function.

Limitations of this work direct several future studies. While the model formulation replicated experimental data very well, the mathematical construct is still restricted to existing expressions of strain-energies. Physically significant parameters, such as branch generation, inner diameter dimensions, or tissue thickness, can directly inform pulmonary-specific constitutive functions constructed from general continuum theories of strain-energy concavity, similar to formulations of cardiovascular-specific material models (3; 29; 34). Such models can imbed phenomenological representations of fiber crimp with resulting material-force conductance, as seen in worm-like chain models or microstructurally motivated constitutive relations (48; 50). As fiber form is expected to be primarily responsible for mechanical function, image-based constitutive models can yield definitive conclusions by informing the statistical crimp distribution and morphology. We are currently investigating such models.

The role of GAG and elastin should also be explored; a relative increase in elastin fibers between the trachea and smaller bronchi (Figure 7) suggests dynamic testing and pentachrome staining would enable measures of the highly deformable elastin structure and visualization of its regional evolution (72). The unidirectional increasing GAG content distally motivates exploration of viscoelasticity through the incorporation of load-history dependency in constitutive models (12). Exploration of pulmonary viscoelasticity may serve as a potential biomarker for disease, as seen for breast tumors (76).

5. Conclusion

The unknown relationship between pulmonary structure and function imposes significant limitations on medical advancements and clinical translation. Lack of experimentally measured lung material properties disconnects the integral impact of air fluid flow on structural tissue motion, impeding a comprehensive understanding of pulmonary mechanics. We present a combined experimental and computational approach to characterize the mechanical behavior of pulmonary airways. The non-linear anisotropic and heterogeneous nature of porcine bronchi is well-captured by an incompressible strain-energy function with fiber-reinforcement. The resulting material behaviors are substantiated by regional dependency of tissue organization caused by structural form and composition, as illustrated by biochemical analysis and histology. Constitutive material property calibrations establish novel airway behavior and put forth a mathematical model representative of multi-regional bronchi response, implying underlying tissue architecture primarily dictates mechanical function.

Our resulting bronchial constitutive law can be directly imbedded in finite element models to explore airway obstruction patterns, design bronchial stents, and facilitate fluid-structure interaction simulations. This foundational study will facilitate investigation of distal airway injury response and progression of pulmonary disease, and help advance lung biomechanics research translation to the clinic through computational techniques.

Acknowledgments

This study was supported in part by the Molecular and Translational Medicine Award from the Entrepreneurial Proof-of-Concept and Innovation Center to Mona Eskandari; and in part by the National Institute of Environmental Health Sciences, National Institutes of Health (NIEHS R00ES025819) to Tara M. Nordgren. We thank the Gladstone Histology and Light Microscopy Core for experimental and technical support for histology.

References

[1]. Al Jamal R; Roughley PJ; Ludwig MS Effect of glycosaminoglycan degradation on lung tissue viscoelasticity. American Journal of Physiology: Lung Cellular and Molecular Physiology. 2001, 280(2), L306–L315. [PubMed: 11159010]

[2]. Andrikakou P; Vickraman K; Arora H On the behaviour of lung tissue under tension and compression. Scientific Reports. 2016, 6, 36642. [PubMed: 27819358]

[3]. Avazmohammadi R; Hill MR; Simon MA; Zhang W; Sacks MS A novel constitutive model for passive right ventricular myocardium: evidence for myofiber-collagen fiber mechanical coupling. Biomechanics and m]Modeling in Mechanobiology. 2017, 16(2), 561–581.

[4]. Bai TR; Knight DA Structural changes in the airways in asthma: observations and consequences. Clinical Science. 2005, 108, 463–477. [PubMed: 15896192]

[5]. Bai A; Eidel DH; Hogg JC; James AL; Lambert RK; Ludwig MS; Martin M; McDonald DM; Mitzner WA; Okazawa M; Pack RJ; Paré PD; Schellenberg RR; Tiddens HA; Wagner EM; Yager D Proposed nomenclature for quantifying subdivisions of the bronchial wall. Journal of Applied Physiology. 1994, 77, 1011–1014. [PubMed: 8002485]

[6]. Barnett SB; Nurmagambetov TA; Costs of asthma in the United States: 2002–2007. Journal of Allergy and Clinical Immunology. 2011, 127, 145–152. [PubMed: 21211649]

[7]. Bentley JP; Hanson AN The hydroxyproline of elastin. Biochimica et Biophysica Acta (BBA)-Protein Structure, 1969, 175(2), 339–344.

[8]. Bezci SE; Nandy A; O'Connell GD Effect of hydration on healthy intervertebral disk mechanical stiffness. Journal of Biomechanical Engineering. 2015, 137(10), 101007. [PubMed: 26300418]

[9]. Bock P; Stockinger L Light and electron microscopic identification of elastic, elaunin and oxytalan fibers in human tracheal and bronchial mucosa. Anatomy and embryology. 1984, 170(2), 145–153. [PubMed: 6517349]

[10]. Budday S; Nay R; de Rooij R; Steinmann P; Wyrobek T; Ovaert TC; Kuhl E Mechanical properties of gray and white matter brain tissue by indentation. Journal of the Mechanical Behavior of Biomedical Materials. 2015, 46, 318–330. [PubMed: 25819199]

[11]. Budday S; Sommer G; Birkl C; Langkammer C; Haybaeck J; Kohnert J; Bauer M; Paulsen F; Steinmann P; Kuhl E; Holzapfel GA Mechanical characterization of human brain tissue. Acta Biomaterialia. 2017, 48, 319–340. [PubMed: 27989920]

[12]. Budday S; Sommer G; Haybaeck J; Steinmann P; Holzapfel GA; Kuhl E Rheological characterization of human brain tissue. Acta Biomaterialia. 2017, 60, 315–329. [PubMed: 28658600]

[13]. Carniel TA; Fancello EA A transversely isotropic coupled hyperelastic model for the mechanical behavior of tendons. Journal of Biomechanics. 2017, 54, 49–57. [PubMed: 28238424]

[14]. Codd SL; Lambert RK; Alley MR; Pack RJ Tensile stiffness of ovine tracheal wall. Journal of Applied Physiology. 1994, 76, 2627–2635. [PubMed: 7928893]

[15]. Devore JL Probability and Statistics for Engineering and The Sciences. Duxbury Press 1991, Belmont, CA.

[16]. Dey P Basic and Advanced Laboratory Techniques in Histopathology and Cytology. Springer 2018.

[17]. Ebihara T; Venkatesan N; Tanaka R; Ludwig MS Changes in extracellular matrix and tissue viscoelasticity in bleomycin-induced lung fibrosis: temporal aspects. American Journal of Respiratory and Critical Care Medicine. 2000 162, 1569–1576. [PubMed: 11029378]

[18]. Ernst A; Herth FJF (Eds). Principles and practice of interventional pulmonology. Springer Science & Business Media 2012.

[19]. Eskandari M; Pfaller MR; Kuhl E On the role of mechanics in chronic lung disease. Materials. 2013, 6, 5639–5658. [PubMed: 28788414]

[20]. Eskandari M; Kuschner WG; Kuhl E Patient-specific airway wall remodeling in chronic lung disease. Annals of Biomedical Engineering. 2015, 10, 2538–2551.

[21]. Eskandari M; Kuhl E Systems biology and mechanics of growth. Wiley Interdisciplinary Reviews: Systems Biology and Medicine. 2015, 7, 401–412. [PubMed: 26352286]

[22]. Eskandari M; Javili A; Kuhl E Elastosis during airway wall remodeling explains multiple coexisting instability patterns. Journal of Theoretical Biology. 2016, 403, 209–218. [PubMed: 27211101]

[23]. Eskandari M; Arvayo AL; Levenston ME Mechanical Properties of the Airway Tree: Heterogeneous and Anisotropic Pseudoelastic and Viscoelastic Tissue Responses. Journal of Applied Physiology. 2018, 125(3), 878–888. [PubMed: 29745796]

[24]. Forum of International Respiratory Societies. The Global Impact of Respiratory Disease, Second Edition Sheffield, European Respiratory Society, 2017 https://www.who.int/gard/publications/TheGlobalImpactofRespiratoryDisease.pdf

[25]. Feng Y; Zhao J; Kleinstreuer C; Wang Q; Wang J; Wu DH; Lin J An in silico Inter-subject Variability Study of Extra-thoracic Morphology Effects on Inhaled Particle Transport and Deposition. Journal of Aerosol Science. 2018, 123, 185–207.

[26]. Fixman ED; Stewart A; Martin JG Basic mechanisms of development of airway structural changes in asthma. European Respiratory Journal. 2007, 292, 379–389. [PubMed: 17264325]

[27]. Fung YC Biomechanics: Mechanical Properties of Living Tissue. New York: Springer-Verlag, 1993.

[28]. Fung YC; Perrone N; Anliker M Biomechanics, its foundations and objectives In Symposium on Biomechanics, its Foundations and Objectives: University of California, San Diego, NJ, Prentice-Hall 1972.

[29]. Gasser TC; Ogden RW; Holzapfel GA Hyperelastic modelling of arterial layers with distributed collagen fibre orientations. Journal of the Royal Society Interface. 2006, 3(6), 15–35.

[30]. Gattinoni L; Carlesso E; Caironi P Stress and strain within the lung. Current Opinion in Critical Care. 2012,18(1), 42–47. [PubMed: 22157254]

[31]. Guerin HA; Elliott DM The role of fiber-matrix interactions in a nonlinear fiber-reinforced strain energy model of tendon. Journal of Biomechanical Engineering. 2005, 127(2), 345–350. [PubMed: 15971713]

[32]. Hogg JC; Chu F; Utokaparch S; Woods R; Elliott WM; Buzatu L; Cherniack RM; Rogers RM; Sciurba FC; Coxson HO; Paré PD The nature of small-airway obstruction in chronic obstructive pulmonary disease. New England Journal of Medicine. 2004, 350, 2645–2653. [PubMed: 15215480]

[33]. Holzapfel GA Biomechanics of soft tissue. The handbook of materials behavior models, 2001, 3(1), 1049–1063.

[34]. Holzapfel GA; Ogden RW Constitutive modelling of passive myocardium: a structurally based framework for material characterization. Philosophical Transactions of the Royal Society of London A: Mathematical, Physical and Engineering Sciences. 2009, 367(1902), 3445–3475.

[35]. Holzapfel GA; Ogden RW Comparison of two model frameworks for fiber dispersion in the elasticity of soft biological tissues. European Journal of Mechanics - A/Solids. 2017, 66, 193–200.

[36]. Hosseini HS; Taber LA How mechanical forces shape the developing eye. Progress in biophysics and molecular biology. 2018, 137, 25–36. [PubMed: 29432780]

[37]. Houghton AM Matrix metalloproteinases in destructive lung disease. Matrix Biology. 2015, 44, 167–174. [PubMed: 25686691]

[38]. Humphrey JD; Yin FCP On constitutive relations and finite deformations of passive cardiac tissue: I. A pseudostrain-energy function. Journal of Biomechanical Engineering. 1987, 109(4), 298–304. [PubMed: 3695429]

[39]. Hurtado DE; Villarroel N; Andrade C; Retamal J; Bugedo G; Bruhn A Spatial patterns and frequency distributions of regional deformation in the healthy human lung. Biomechanics and Modeling in Mechanobiology. 2017, 16(4), 1413–1423. [PubMed: 28315975]

[40]. Iatridis JC; Kumar S; Foster RJ; Weidenbaum M; Mow VC Shear mechanical properties of human lumbar annulus fibrosus. Journal of Orthopaedic Research. 1999, 17(5), 732–737. [PubMed: 10569484]

[41]. James AL; Paré PD; Hogg JC; The mechanics of airway narrowing in asthma. American Review of Respiratory Disease. 1989, 139, 242–246. [PubMed: 2912345]

[42]. Jeffery PK Remodeling in asthma and chronic obstructive lung disease. American Journal of Respiratory and Critical Care Medicine. 2001, 164, S28–S38. [PubMed: 11734464]

[43]. Jesudason R; Sato S; Parameswaran H; Araujo AD; Majumdar A; Allen PG; Bartolák-Suki E; Suki B Mechanical forces regulate elastase activity and binding site availability in lung elastin. Biophysical Journal. 2010, 99(9), 3076–3083. [PubMed: 21044606]

[44]. Kamel KS; Beckert LE; Stringer MD Novel insights into the elastic and muscular components of the human trachea. Clinical Anatomy. 2009, 22(6), 689–697. [PubMed: 19637300]

[45]. Kamm RD Airway wall mechanics. Ann Rev Biomed Eng. 1999, 1, 47–72. [PubMed: 11701482]

[46]. Kannan R; Guo P; Przekwas A Particle transport in the human respiratory tract: formulation of a nodal inverse distance weighted Eulerian-Lagrangian transport and implementation of the Wind-Kessel algorithm for an oral delivery. International Journal for Numerical Methods in Biomedical Engineering. 2016, 32(6), e02746.

[47]. Kannan R; Singh N; Przekwas A; A Quasi-3D compartmental multi-scale approach to detect and quantify diseased regional lung constriction using spirometry data. International Journal for Numerical Methods in Biomedical Engineering. 2018, 34(5), e2973. [PubMed: 29486525]

[48]. Kuhl E; Garikipati K; Arruda EM; Grosh K Remodeling of biological tissue: mechanically induced reorientation of a transversely isotropic chain network. Journal of the Mechanics and Physics of Solids. 2005, 53(7), 1552–1573.

[49]. Lambert RK; Wilson TA; Hyatt RE; Rodarte JR A computational model for expiratory flow. Journal of Applied Physiology. 1982, 52(1), 44–56. [PubMed: 7061277]

[50]. Lanir YT Constitutive equations for fibrous connective tissues. Journal of Biomechanics. 1983, 16(1), 1–12. [PubMed: 6833305]

[51]. Lee T; Sergey YT; Arun KG; Ilias B; Buganza Tepole, A. Propagation of material behavior uncertainty in a nonlinear finite element model of reconstructive surgery. Biomechanics and Modeling in Mechanobiology. 2018, 17(6), 1857–1873. [PubMed: 30073612]

[52]. Lutchen KR; Paré PD; Seow CY Hyperresponsiveness: relating the intact airway to the whole lung. Physiology. 2017, 32(4), 322–331. [PubMed: 28615315]

[53]. Mead-Hunter R; King AJ; Larcombe AN; Mullins BJ The influence of moving walls on respiratory aerosol deposition modelling. Journal of Aerosol Science. 2013, 64, 48–59.

[54]. Masri C; Chagnon G; Favier D; Sartelet H; Girard E Experimental characterization and constitutive modeling of the biomechanical behavior of male human urethral tissues validated by histological observations. Biomechanics and Modeling in Mechanobiology. 2017, 1–12.

[55]. Mauad T; Xavier A Elastosis and fragmentation of fibers of the elastic system in fatal asthma. American Journal of Respiratory and Critical Care Medicine. 1999, 160, 968–975. [PubMed: 10471626]

[56]. Moulton DE; Goriely A Possible role of differential growth in airway wall remodeling in asthma. Journal of Applied Physiology. 2011, 110, 1003–1012. [PubMed: 21252217]

[57]. McKay KO; Wiggs BR; Paré PD; Kamm RD Zero-stress state of intra-and extraparenchymal airways from human, pig, rabbit, and sheep lung. Journal of Applied Physiology. 2002, 92(3), 1261–1266. [PubMed: 11842066]

[58]. Noble PB; Turner DJ; Mitchell HW Relationship of airway narrowing, compliance, and cartilage in isolated bronchial segments. Journal of Applied Physiology. 2002, 92(3), 1119–1124. [PubMed: 11842048]

[59]. Noble PB; Sharma A; McFawn PK; Mitchell HW Airway narrowing in porcine bronchi with and without lung parenchyma. European Respiratory Journal. 2005, 26(5), 804–811. [PubMed: 16264040]

[60]. Noble PB; Sharma A; McFawn PK; Mitchell HW Elastic properties of the bronchial mucosa: epithelial unfolding and stretch in response to airway inflation. Journal of Applied Physiology. 2005, 99(6), 2061–2066. [PubMed: 16024520]

[61]. Noble PB; Hernandez JM; Mitchell HW; Janssen LJ Deep inspiration and airway physiology: human, canine, porcine, or bovine? Journal of Applied Physiology. 2010, 109(3), 938–939. [PubMed: 20829504]

[62]. Oakes JM; Shadden SC; Grandmont C; Vignon Clementel IE Aerosol Transport Throughout Inspiration and Expiration in the Pulmonary Airways. International Journal for Numerical Methods in Biomedical Engineering. 2016 33(9), e2847.

[63]. O'Connell GD; Guerin HL; Elliott DM Theoretical and uniaxial experimental evaluation of human annulus fibrosus degeneration. Journal of Biomechanical Engineering. 2009, 31(11), 111007.

[64]. O'Connell GD Degeneration affects the structural and tissue mechanics of the intervertebral disc. 2009.

[65]. O'Connell GD; Sen S; Elliott DM Human annulus fibrosus material properties from biaxial testing and constitutive modeling are altered with degeneration. Biomechanics and Modeling in Mechanobiology. 2011, 11(3–4), 493–503. [PubMed: 21748426]

[66]. Peng X; Madany AM; Jang JC; Valdez JM; Rivas Z; Burr AC; Grinberg YY; Nordgren TM; Nair MG; Cocker D; Carson MJ Continuous Inhalation Exposure to Fungal Allergen Particulates Induces Lung Inflammation While Reducing Innate Immune Molecule Expression in the Brainstem. American Society for Neurochemistry: Neuro. 2018, 10, 1759091418782304.

[67]. Perlman CE; Bhattacharya J Alveolar expansion imaged by optical sectioning microscopy. Journal of Applied Physiology. 2017, 103(3), 1037–1044.

[68]. Polzer S; Gasser TC; Novak K; Man V; Tichy M; Skacel P; Bursa J Structure-based constitutive model can accurately predict planar biaxial properties of aortic wall tissue. Acta Biomaterialia. 2015, 14, 133–145. [PubMed: 25458466]

[69]. Quanjer PH; Tammeling GJ; Cotes JE; Pedersen OF; Peslin R, Yernault J Lung volumes and forced ventilatory flows. European Respiratory Journal. 1993, 5–40.

[70]. Rattue P Lung Diseases Leading Cause Of Death, Most People Don't Know Medical News Today, MediLexicon International 2012, www.medicalnewstoday.com/articles/247293.php.

[71]. Razavi MJ; Pidaparti R; Wang X Surface and interfacial creases in a bilayer tubular soft tissue. Physical Review E. 2016, 94, 022405. [PubMed: 27627333]

[72]. Reddel CJ; Weiss AS; Burgess JK Elastin in asthma. Pulmonary Pharmacology and Therapeutics. 2012, 25(2), 144–153. [PubMed: 22366197]

[73]. Sacks MS Biaxial mechanical evaluation of planar biological materials. Journal of Elasticity and the Physical Science of Solids. 2000, 61(1–3), 199.

[74]. Safshekan F; Tafazzoli-Shadpour M; Abdouss M; Shadmehr MB Mechanical characterization and constitutive modeling of human trachea: age and gender dependency. Materials. 2016, 9(6), 456.

[75]. Shapiro SD; Ingenito EP The pathogenesis of chronic obstructive pulmonary disease: advances in the past 100 years. American Journal of Respiratory Cell and Molecular Biology. 2005, 325, 367–372. [PubMed: 15837726]

[76]. Sinkus R; Siegmann K; Xydeas T; Tanter M; Claussen C; Fink M MR elastography of breast lesions: understanding the solid/liquid duality can improve the specificity of contrast-enhanced MR mammography. Magnetic Resonance in Medicine: An Official Journal of the International Society for Magnetic Resonance in Medicine. 2007, 58(6), 1135–1144.

[77]. Starcher BC Elastin and the lung. Thorax. 1986, 41(8), 577. [PubMed: 3538485]

[78]. Suki B; Bates JH Lung tissue mechanics as an emergent phenomenon. Journal of Applied Physiology. 2011 110(4), 1111–1118. [PubMed: 21212247]

[79]. Spencer AJM Constitutive Theory for Strongly Anisotropic Solids. Continuum Theory of the Mechanics of Fibre-Reinforced Composites Springer, Vienna 1984, 1–32.

[80]. Tartibi M; Steigmann DJ; Komvopoulos K An inverse finite element method for determining residual and current stress fields in solids. Computational Mechanics. 2016, 58(5), 797–817.

[81]. Teng Z; Trabelsi O; Ochoa I; He J; Gillard JH; Doblare M Anisotropic material behaviours of soft tissues in human trachea: an experimental study. Journal of Biomechanics. 2012, 45(9), 1717–1723. [PubMed: 22534565]

[82]. Trabelsi O; Del Palomar AP; Lopez-Villalobos JL; Ginel A; Doblare M Experimental characterization and constitutive modeling of the mechanical behavior of the human trachea. Medical Engineering and Physics, 2010, 32(1), 76–82. [PubMed: 19926513]

[83]. Vawter DL; Fung YC; West JB Constitutive equation of lung tissue elasticity. Journal of Biomechanical Engineering. 1979, 101(1), 38–45.

[84]. Wagner DR; Lotz JC Theoretical model and experimental results for the nonlinear elastic behavior of human annulus fibrosus. Journal of orthopaedic research. 2004, 22(4), 901–909. [PubMed: 15183453]

[85]. Wall WA; Rabczuk T Fluid–structure interaction in lower airways of CT-based lung geometries. International Journal for Numerical Methods in Fluids. 2008, 57(5), 653–675.

[86]. Werbner B; Zhou M; O'Connell G A novel method for repeatable failure testing of annulus fibrosus. Journal of Biomechanical Engineering. 2017, 139(11), 111001.

[87]. Wiggs BR; Hrousis CA; Drazen JM; Kamm RD On the mechanism of mucosal folding in normal and asthmatic airways. Journal of Applied Physiology. 1997, 83, 1814–1821. [PubMed: 9390950]

[88]. Wiechert L; Comerford A; Rausch S; Wall W Advanced multi-scale modelling of the respiratory system. Fundamental Medical and Engineering Investigations on Protective Artificial RespirationSpringer, Berlin, Heidelberg 2011, 116, 1–32.

[89]. Wilson L; Devine EB; So K Direct medical costs of chronic obstructive pulmonary disease: chronic bronchitis and emphysema. Respiratory Medicine. 2000, 83, 204–213.

[90]. Xi J; Longest PW Transport and deposition of micro-aerosols in realistic and simplified models of the oral airway. Annals of Biomedical Engineering. 2017, 35(4), 560–581.

[91]. Yang L; Li J; Mo H; Pidaparti RM; Witten TM Possible role of collagen reorientation during airway remodeling on mucosal folding. Journal of Engineering Mathematics. 2015, 96(1), 37–56.

[92]. Yang W; Vincent SR; Gludovatz B; Schaible E; Stewart P; Ritchie RO; Meyers MA On the tear resistance of skin. Nature Communications. 2015, 6, 6649.

[93]. Yin Y; Choi J; Hoffman EA; Tawhai MH; Lin CL Simulation of pulmonary air flow with a subject-specific boundary condition. Journal of Biomechanics. 2010, 43(11), 2159–2163. [PubMed: 20483412]

[94]. Yoshihara L; Ismail M; Wall WA Bridging scales in respiratory mechanics. Computer Models in Biomechanics Springer, Dordrecht 2013, 395–407.

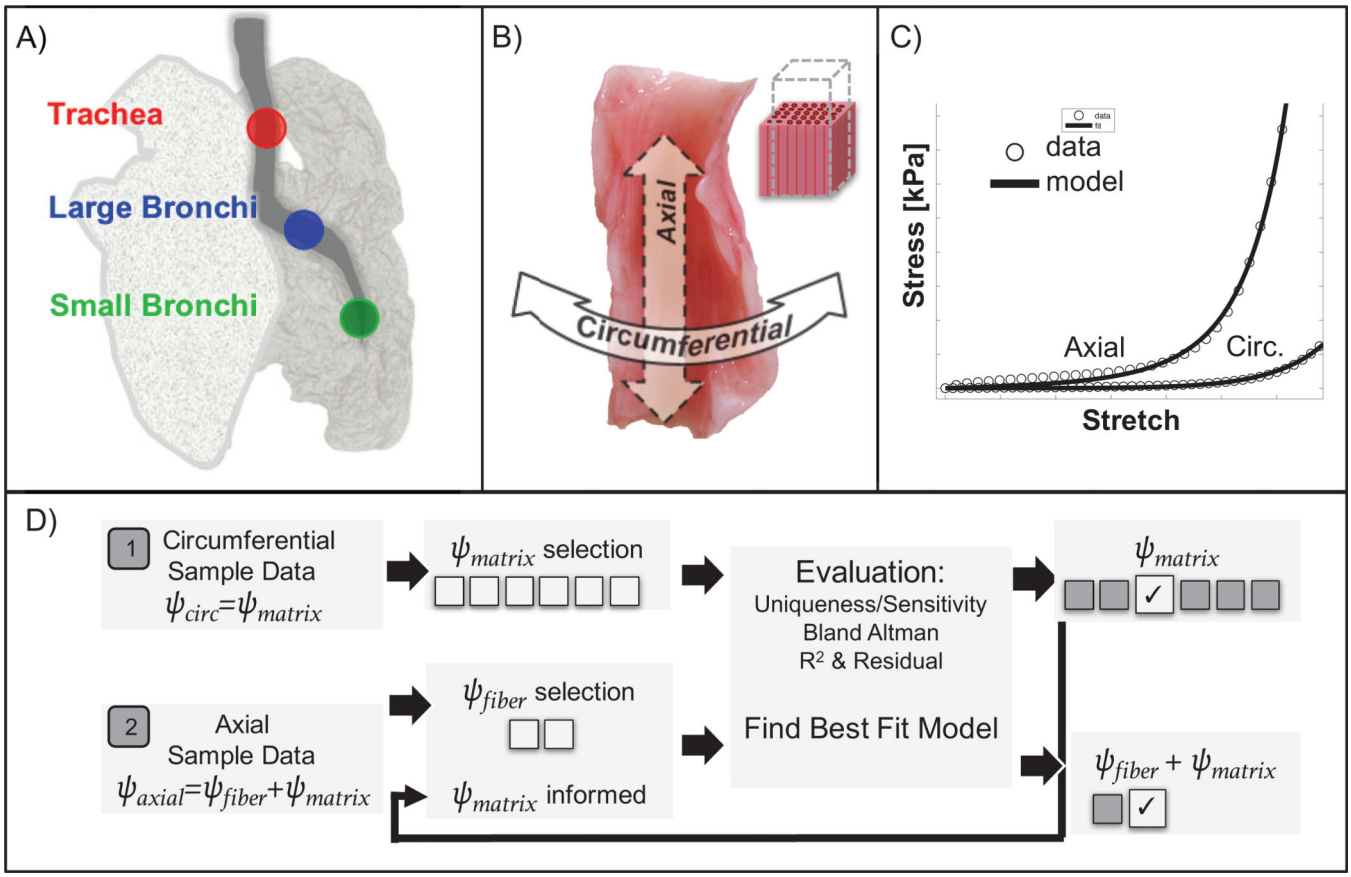

Figure 1:

Schematic of study design. A) Three regions of porcine airway were evaluated, including trachea, large bronchi, and small bronchi. B) For each region, samples were orientated along the circumferential or axial direction, with fibers aligned along the axial direction. C) The stress-strain response was curve-fit to a structure-based constitutive model that included a description for the fibers and extrafibrillar matrix. D) Methods for model selection, whereby circumferential samples informed the matrix model, which was combined with a fiber model to fit axial samples.

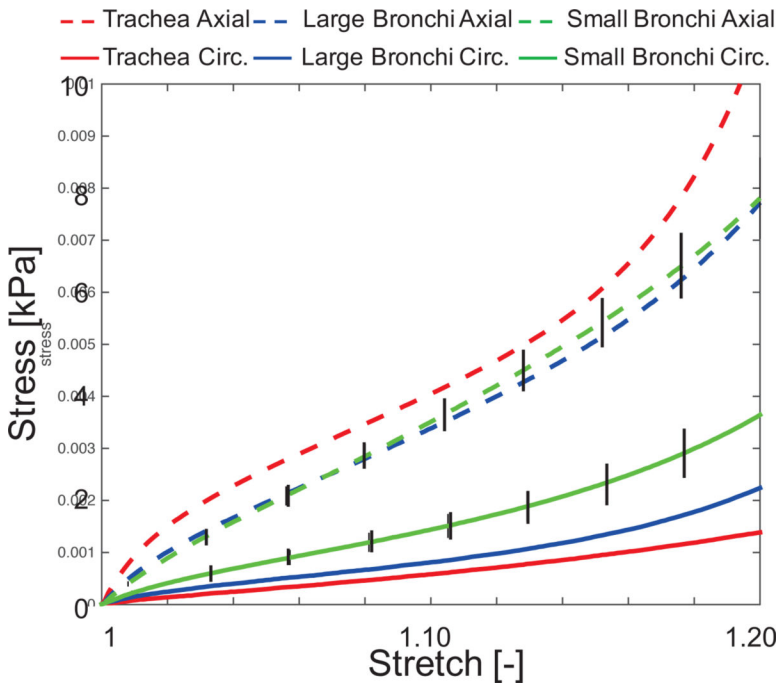

Figure 2:

Average stress-stretch curves for each sample orientation and region. Generally, axial samples displayed greater strain-stiffening than circumferential samples. For clarity, standard error of the mean is shown for the small bronchi.

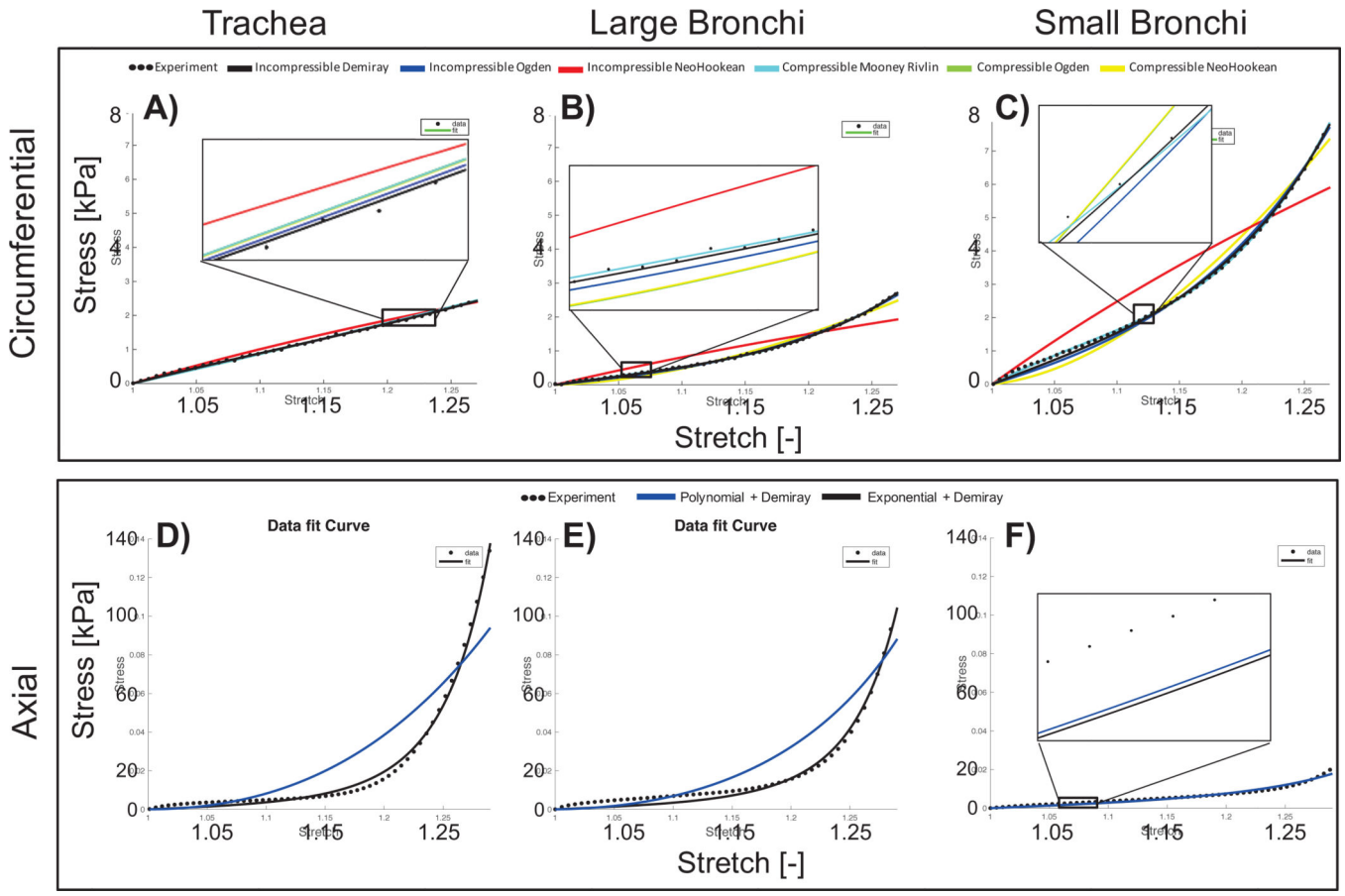

Figure 3:

Representative uniaxial stress-stretch data of circumferential (A-C) and axial (D-F) specimens fit to various constitutive models. Model parameters were fit for each region separately (A and D: trachea, B and E: large bronchi, C and F: small bronchi). Circumferential samples were fit to homogenous compressible and incompressible non-linear matrix models, with incompressible Demiray providing the best fit based on high R^2, low residual error, and sensitivity analysis (top row, black line). Axial tissues were fit to fiber-reinforced exponential or polynomial function, with incompressible Demiray for the matrix. Fibers were best described with an exponential strain-energy function (bottom row, black line). Incompressible NeoHookean (black line, B-C) and polynomial model (blue line, D-E) poorly represented experimental data. Comparable fit performances are visible in reduced stress-strain range insets.

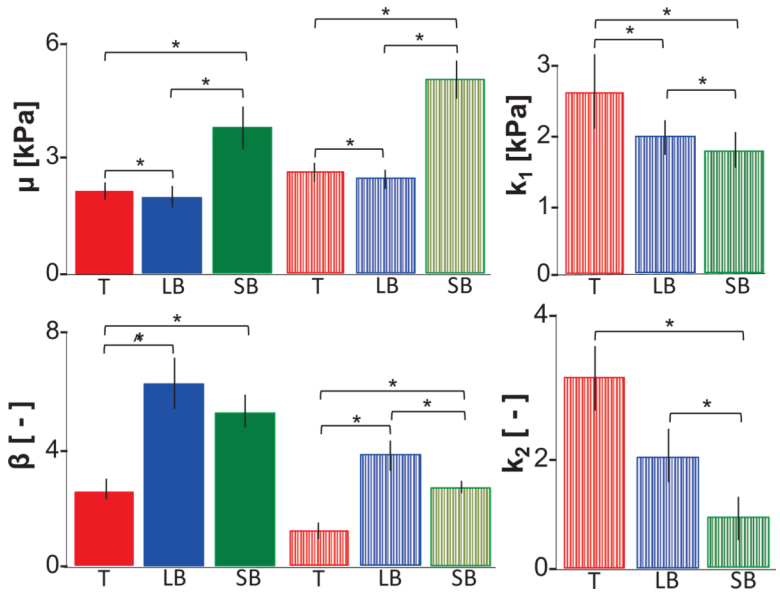

Figure 4:

Average ± standard error of means of incompressible Demiray model parameters (μ, β, k_1 and k_2) determined by fit to circumferentially oriented samples (solid bars) or in combination with a fiber description for axially-oriented samples (striped bars). Regional differences for μ and β were similar for both circumferentially and axially oriented specimens (trachea (T), large bronchi (LB), and small bronchi (SB)). k_1 and k_2 fiber parameters were determined from axially oriented specimens. Regional differences were observed for both fiber parameters. *p<0.001, ^p=0.003.

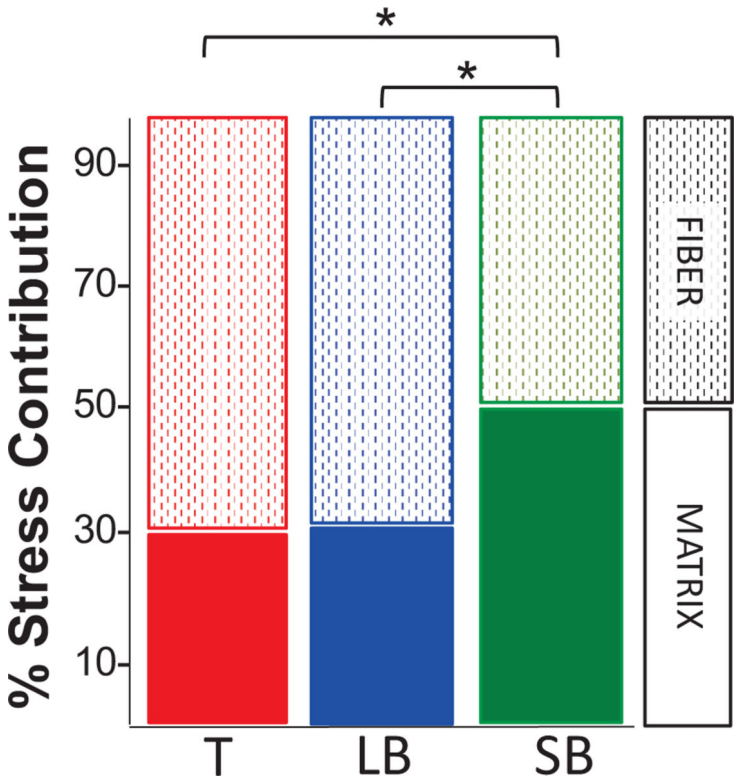

Figure 5:

Percent stress contribution from fiber (dotted lined bars)and matrix (solid bars) components. Fiber contribution was greater than the matrix contribution in the trachea (T) and large bronchi (LB). Stress contribution was evenly distributed between matrix and fibers in the small bronchi (SB). *$p<0.002$.

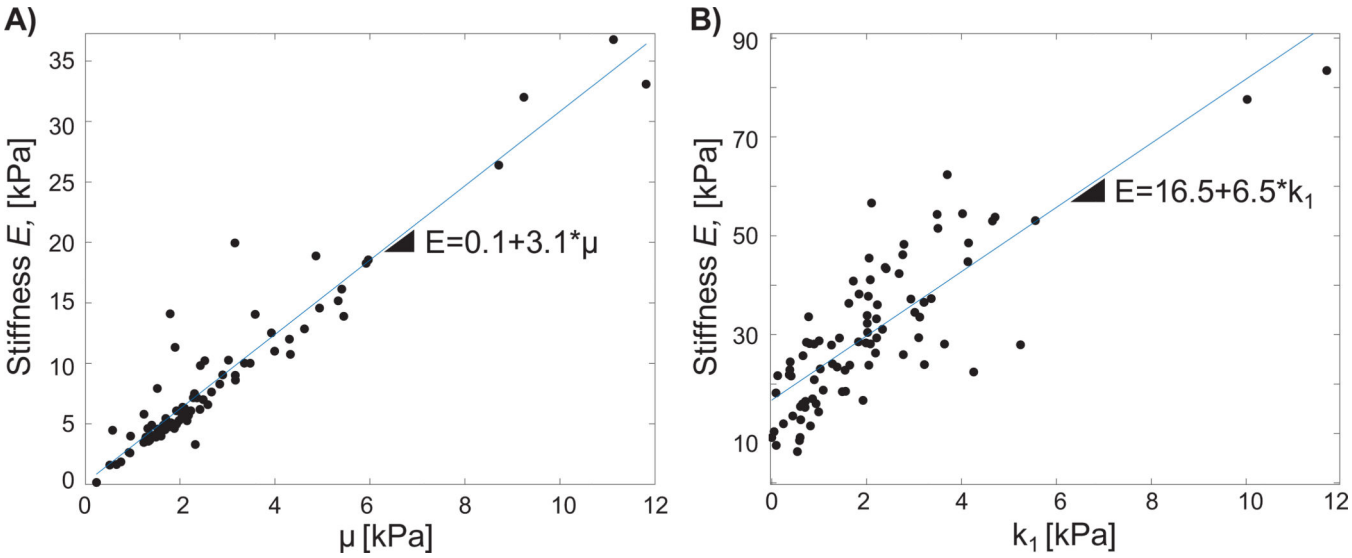

Figure 6:

A) For circumferential samples, a strong correlation was observed between bulk tissue modulus E and matrix modulus μ. B) For axial samples, a strong correlation was observed between bulk tissue modulus and fiber stiffness k_1. Data for all three regions shown.

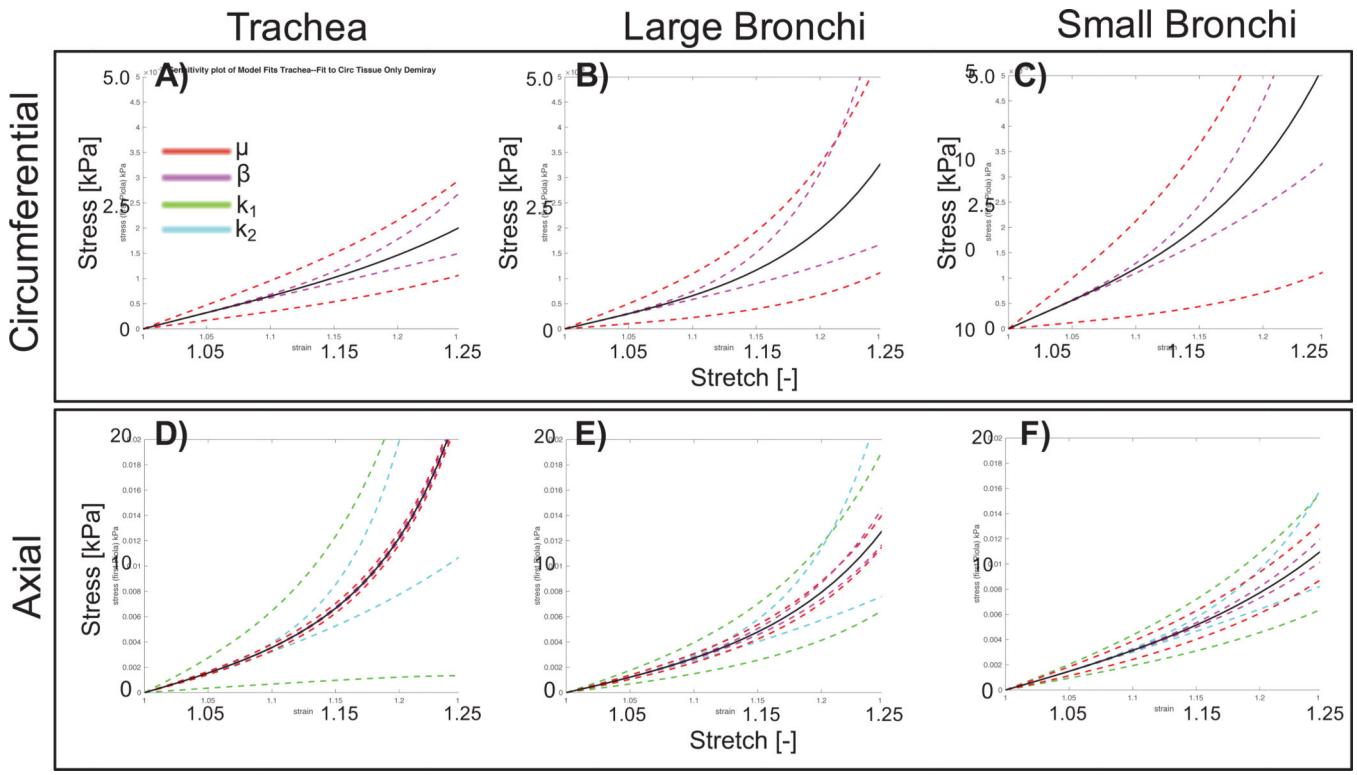

Figure 7:

Results from sensitivity analysis. A-C) Incompressible Demiray model shown with average model parameters represented by the solid black line. Deviations in model parameters μ, β by ± 1 standard deviation are shown by colored dashed lines. D-F) Combined exponential fiber and incompressible Demiray matrix fit with average model parameters (solid black line) and deviations of μ, β, k_1, k_2 by ± 1 standard deviation. One parameter was varied (colored, dotted lines) while others were held fixed to the average value.

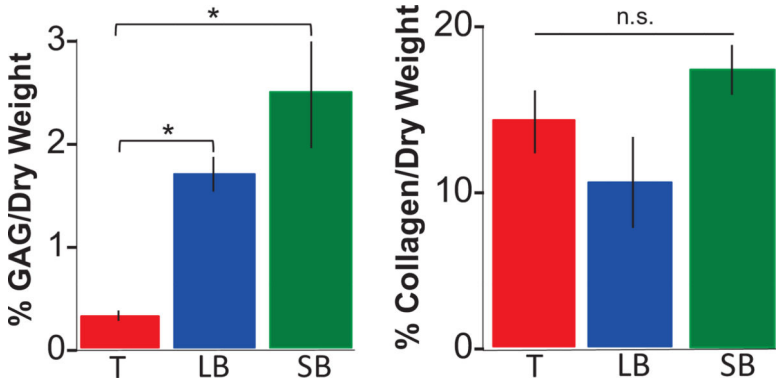

Figure 8:

Glycosaminoglycans (GAG) and collagen content of soft tissue (submucosa and mucosa) normalized by dry weight (average ± standard deviation for all three regions: trachea (T), large bronchi (LB) and small bronchi (SB)). Generally, GAG and DNA content increased from proximal to distal regions (*$p<0.001$). Conversely, regional differences were not significant (n.s.) for collagen content.

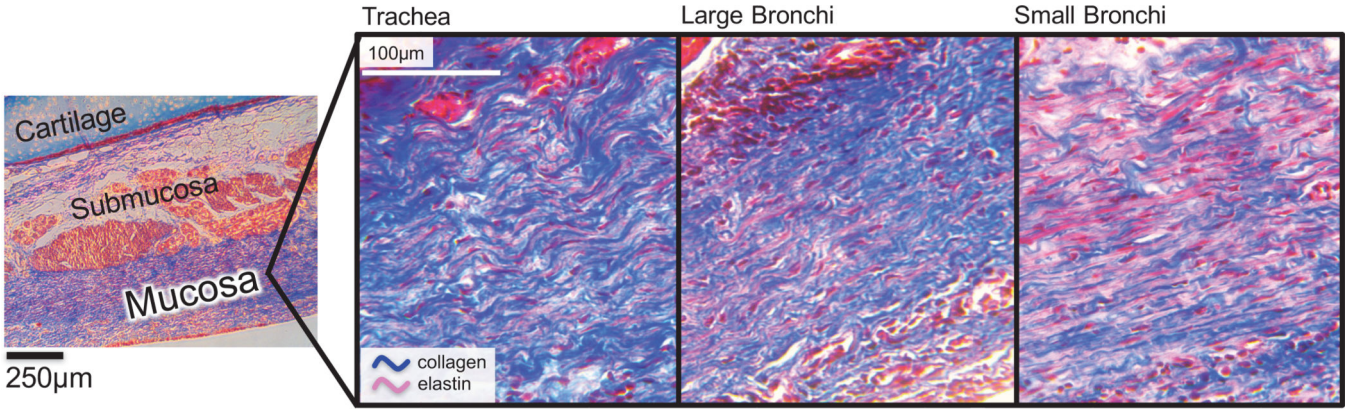

Figure 9:

Representative histological samples stained with Masson's Trichrome, where collagen fibers are blue and elastin fibers appear red. Fibers in the trachea were crimped, while fibers in the small bronchi appeared to be taut and straightened.

Table 1:

Table of strain-energy density functions (SED) used to describe extrafibrillar matrix (circumferentially oriented samples) and fiber (axially oriented samples) mechanics.

Model Name	SED (ψ)	Function of Stretch (λ_3)	Parameters [Units] and Definitions
Compressible NeoHookean $\psi(I_1(\lambda_3), J(\lambda_3))$	$\frac{1}{2}\mu[I_1-3]+\frac{\lambda}{2}\ln(J)^2-\mu\ln(J)$	$I_1=\mathrm{tr}(C)=2\lambda_3^{-2\nu}+\lambda_3^2$ $J=\det(F)=\lambda_3^{1-2\nu}$ I_1 first invariant, J Jacobian	λ [MPa], Lamé constant μ [kPa], Lamé constant ν [−], Poisson's Ratio
Unconstrained Ogden $\psi(\lambda_3, a(\lambda_3))$	$\frac{1}{2}c_p(J-1)^2$ $+\frac{c_1}{\alpha^2}\left(\lambda_1^\alpha+\lambda_2^\alpha+\lambda_3^\alpha-\alpha\ln(J)\right)$	$\lambda_1=\lambda_2=\lambda_3^{-\nu}$ $J=\det(F)=\lambda_3^{1-2\nu}$ J Jacobian	c_1 [kPa], coefficient c_p [MPa], bulk-like modulus α [−], exponent ν [−], Poisson's Ratio
Uncoupled Mooney Rivlin $\psi(I_1(\lambda_3), I_2(\lambda_3)J(\lambda_3))$	$c_1(I_1-3)+c_2(I_2-3)$ $-2(c_1+2c_2)\ln(J)+\frac{\lambda}{2}\ln(J)^2$	$J=\det(F)=\lambda_3^{1-2\nu}$ $I_1=\mathrm{tr}(C)=2\lambda_3^{-2\nu}+\lambda_3^2$ $I_2=\frac{1}{2}\left[(\mathrm{tr}(C))^2+\mathrm{tr}\left(C^2\right)\right]=$ $=\lambda_3^{-4\nu}+2\lambda_3^{(2-2\nu)}$ I_1 first invariant, I_2 second invariant, J Jacobian	c_1 [MPa], coefficient c_2 [MPa], coefficient λ [MPa], coefficient ν [−], Poisson's Ratio
Incompressible Ogden $\psi(I_1\lambda_1(\lambda_3), \lambda_2(\lambda_3))$	$\frac{2\mu}{\alpha^2}\left(\lambda_1^\alpha+\lambda_2^\alpha+\lambda_3^\alpha-3\right)$	$I_1=\mathrm{tr}(C)=2\lambda_3^{-2\nu}+\lambda_3^2$	α [−], exponent μ [kPa], coefficient
Incompressible Demiray $\psi(I_1(\lambda_3))$	$\frac{\mu}{2\beta}(\exp[\beta(I_1-3)]-1)$	$I_1=\mathrm{tr}(C)=2\lambda_3^{-2\nu}+\lambda_3^2$ I_1 first invariant	β [−], exponent μ [kPa], coefficient
Incompressible NeoHookean $\psi(I_1(\lambda_3))$	$\frac{\mu}{2}(I_1-3)$	$I_1=\mathrm{tr}(C)=2\lambda_3^{-2\nu}+\lambda_3^2$ I_1 first invariant	μ [kPa], coefficient
Exponential $\psi(I_4(\lambda_3))$	$\frac{k_1}{k_2}\left(\exp\left[k_2(I_4-1)^2\right]-1\right)$	$I_4=\lambda_3^2$	k_1 [kPa], coefficient k_2 [−], exponent
Polynomial $\psi(I_4(\lambda_3))$	$k_1(I_4-1)^2+k_2(I_4-1)^3$	$I_4=\lambda_3^2$	k_1 [kPa], coefficient k_2 [kPa], coefficient

Table 2:

Model parameters from curve-fitting. All models were evaluated for parameter uniqueness, sensitivity, reproducibility, and agreement between model fit and experimental data (greater R^2 coefficient and lower residual error). Models highlighted in green satisfied these criteria, while yellow yielded non-unique fits, and orange denoted a poor fit.

Matrix Response (Circumferential Samples)							
Compressible Models				*Incompressible Models*			
Neohookean				Ogden			
R^2=0.964, Residual [Mpa]=−0.131	Trachea	Large Bronchi	Small Bronchi	R^2=0.995, Residual [Mpa]=−0.088	Trachea	Large Bronchi	Small Bronchi
ν[−]	0.48 ± 0.07	0.48 ± 0.07	0.48 ± 0.06	μ[*kPa*]	3.80 ± 2.13	2.58 ± 1.80	5.45 ± 4.55
μ[*kPa*]	23.7 ± 39.3	147 ± 298	115 ± 166	α[−]	7.64 ± 3.60	13.8 ± 9.34	12.0 ± 5.57
λ[*MPa*]	−1120 ± 1110	−3760 ± 4920	−3250 ± 3340				
Unconstrained Ogden				Demiray			
R^2=0.964, Residual [Mpa]=−0.131	Trachea	Large Bronchi	Small Bronchi	R^2=0.997, Residual [Mpa]=−0.041	Trachea	Large Bronchi	Small Bronchi
ν[−]	0.34 ± 0.09	0.25 ± 0.14	0.24 ± 0.12	μ[*kPa*]	2.21 ± 1.04	2.02 ± 1.33	3.76 ± 2.95
c_p [Mpa]	39.5 ± 245	11.2 ± 49.7	8.86 ± 44.0	β[−]	2.51 ± 1.83	6.19 ± 4.21	5.17 ± 2.89
c_1 [kPa]	127 ± 842	−287 ± 932	−322 ± 409				
α[−]	−8.68 ± 36.3	2.05 ± 4.12	0.36 ± 7.56				
Uncoupled Mooney-Rivlin				Incompressible Neohookean			
R^2=0.963, Residual [Mpa]=−0.125	Trachea	Large Bronchi	Small Bronchi	R^2=0.819, Residual [Mpa]=0.387	Trachea	Large Bronchi	Small Bronchi
ν[−]	0.42 ± 0.06	0.44 ± 0.09	0.44 ± 0.09	μ[*kPa*]	3.55 ± 2.54	9.35 ± 15.0	10.1 ± 11.1
c_1 [Mpa]	23.9 ± 66.7	452 ± 1820	965 ± 4000				
c_2 [Mpa]	−17.3 ± 90.1	−623 ± 3120	−1560 ± 6940				
λ[*MPa*]	−499 ± 998	−2670 ± 5310	−1910 ± 2980				
Fiber + Matrix Response (Axial Samples)							
Exponential + Demiray				Polynomial + Demiray			
R^2=0.991, Residual [Mpa]=−0.175	Trachea	Large Bronchi	Small Bronchi	R^2=0.959, Residual [Mpa]=0.607	Trachea	Large Bronchi	Small Bronchi
k_1 [*kPa*]	2.61 ± 2.69	1.94 ± 1.22	1.72 ± 1.26	k_1[*kPa*]	2.07 ± 2.83	3.29 ± 3.05	3.76 ± 2.87
k_2 [−]	3.42 ± 2.80	2.01 ± 2.34	0.90 ± 1.85	k_2[*kPa*]	11.5 ± 18.4	2.26 ± 5.00	0.65 ± 1.86
μ[*kPa*]	2.68 ± 0.91	2.51 ± 1.15	5.06 ± 2.44	μ[*kPa*]	2.35 ± 1.01	2.65 ± 1.11	4.18 ± 2.51
β[−]	1.20 ± 1.26	3.74 ± 3.12	2.65 ± 1.22	β[−]	3.49 ± 1.43	7.12 ± 3.88	3.73 ± 2.36

Table 3:

Correlations (ρ), between parameters (interparameter), and between model coefficients and measured mechanical properties. No significant interparameter correlations were observed, except for a weak correlation between β and k_2 (ρ=−0.25). E was significantly correlated with mechanical parameters: for circumferential samples, both μ and β had significant relationships to E, but only μ had a strong correlation (ρ=0.91); similarly for axial samples, μ and k_1 were significantly correlated with E, but only k_1 had a strong correlation coefficient (ρ=0.79).

Incompressible Demiray (Circumferential)		
		Interparameter Correlation
	ρ	p-value
β, μ	0.01	0.94
		Correlation to Stiffness (E)
	ρ	p-value
E, β	0.26	0.02
E, μ	0.91	0.00
Incompressible Demiray + Exponential Fiber (Axial)		
		Interparameter Correlation
	ρ	p-value
β, μ	0.02	0.89
μ, k_1	−0.06	0.56
μ, k_2	−0.16	0.15
β, k_1	0.11	0.30
β, k_2	−0.25	0.02
k_1, k_2	−0.06	0.57
		Correlation to Stiffness (E)
	ρ	p-value
E, μ	0.43	0.00
E, β	0.07	0.52
E, k_1	0.79	0.00
E, k_2	−0.07	0.50